

## Fabrication of $\beta$ -MnO<sub>2</sub>/RGO Composite and Its Electrochemical Properties

Lei Zhang<sup>1</sup>, Hongdong Liu<sup>2,\*</sup>, Haibo Ruan<sup>2</sup>, Yongyao Su<sup>2</sup>, Rong Hu<sup>2</sup>, Liangliang Tian<sup>2</sup>,  
Zhongli Hu<sup>2</sup>, Jing Li<sup>2</sup>

<sup>1</sup> College of life science, Chongqing normal university, Chongqing 401331, PR China

<sup>2</sup> Research institute for new materials technology, Chongqing university of arts and sciences,  
Chongqing 402160, PR China

\*E-mail: [lhd0415@126.com](mailto:lhd0415@126.com)

Received: 25 September 2016 / Accepted: 19 October 2016 / Published: 10 November 2016

---

MnO<sub>2</sub> is considered to be a promising alternative anode material for lithium ion batteries. In this work,  $\beta$ -MnO<sub>2</sub>/RGO composite has been successfully fabricated via hydrothermal method. The sample is carefully investigated by X-ray diffraction (XRD) techniques, Raman spectra, X-ray photoelectron spectroscopy (XPS) and scanning electron microscopy (SEM). When  $\beta$ -MnO<sub>2</sub>/RGO composite as anode material for lithium ion batteries, which shows good cycling performance and excellent rate capacity.

---

**Keywords:** MnO<sub>2</sub>,  $\beta$ -MnO<sub>2</sub>/RGO composite, lithium ion batteries, anode material

### 1. INTRODUCTION

Lithium ion batteries (LIBs) have been the most extensively used power sources for portable electronics and hybrid electric vehicles owing to their high energy density, long cycling life and low production cost [1-3]. In the last decades, graphite has been the traditional commercial anode material for LIBs with its natural abundance and excellent electrical conductivity [4]. However, it still suffers shortcomings of low theoretical specific capacity of 372 mAh g<sup>-1</sup> and poor rate performance, which is far from adequate to meet the demands of the upcoming markets of the portable electronic devices and electrical vehicles [5-7]. In order to enhance capacity and power density, great efforts have been made to develop new electrode materials [8, 9].

MnO<sub>2</sub> stands out among the new alternative materials due to its high theoretical capacities of 1230 mAh g<sup>-1</sup>, excellent residual energy performance, natural abundance, low cost and eco-

friendliness, which has aroused a great interest of the investigator home and abroad [10,11]. When the basic unit  $[\text{MnO}_6]$  octahedral is linked in different ways,  $\text{MnO}_2$  can exist in various crystallographic forms such as  $\alpha$ ,  $\beta$ ,  $\gamma$ ,  $\delta$ ,  $\lambda$  and  $\epsilon$  type [12-14]. The properties of  $\text{MnO}_2$  largely depend on its crystallographic nature [15,16]. Until now,  $\alpha$ -,  $\beta$ -,  $\gamma$ - and  $\delta$ - $\text{MnO}_2$  have been prepared in various morphologies, such as wires, rods, belts, and tubes [17]. Because of various crystallographic structures,  $\text{MnO}_2$  has been widely used in molecular sieve, catalyst, and electrode material in lithium ion batteries as well as in supercapacitors [18]. Among which  $\beta$ - $\text{MnO}_2$  has best thermodynamic stability and is easy to be obtained. Compared to the other  $\text{MnO}_2$ ,  $\beta$ - $\text{MnO}_2$  has a rutile-type tetragonal symmetry ( $P4_2/mnm$ ) with a distorted hexagonal-close packed oxygen array, where edge-sharing  $\text{MnO}_6$  octahedra stacks and forms  $1 \times 1$  ( $0.23 \text{ nm} \times 0.23 \text{ nm}$ ) tunnels [19].  $\beta$ - $\text{MnO}_2$  has received much attention in lithium batteries and showed good performances [20]. Despite the high theoretical capacity, the commercial applications of the  $\text{MnO}_2$ -based anode materials is greatly hampered due to the large loss of reversible capacity, poor cycling stability and residual capacity performance, which is believed to be caused by the pulverization and secondary aggregation owing to the huge volume change of  $\text{MnO}_2$  during discharge/charge process [21-23]. To mitigate these problems, several strategies have been proposed, such as designing various  $\text{MnO}_2$  nanostructures, fabricating  $\text{MnO}_2/\text{C}$  composites and synthesising a specific morphology of  $\text{MnO}_2$  with a large surface area [24, 25]. Among the three methods, the main is to fabricate  $\text{MnO}_2/\text{C}$  composites which can effectively shorten the diffusion distance of lithium ion and provide abundant channels for ions and electrons transport, thus greatly improve the electrochemical property owing to the large specific area mesoporous structures [26]. Compared with the carbon material, the reduced graphene oxide (RGO) as a new-star carbon material possesses all the strongpoints of carbon material, meanwhile, has a better electrochemical property [27].

Therefore, in this paper, we report a green and facile method to prepare  $\beta$ - $\text{MnO}_2/\text{RGO}$  composite by RGO supported  $\beta$ - $\text{MnO}_2$ , which could be improve the electrochemical performance. Because the RGO not only assists relieve the volume change, but also provides high surface area and pore volume to facilitate the electron and ion transfer, the composite exhibits excellent electrochemical performance compared the bare  $\beta$ - $\text{MnO}_2$ .

## 2. EXPERIMENTAL

### 2.1 Synthesis of RGO

Nanostructure graphene oxide (GO) was prepared using the modified Hummers method from flake graphite. First of all, 2 g of natural graphite and 0.8 g of sodium nitrate ( $\text{NaNO}_3$ , 99%) were dissolved in 96 mL concentrated sulphuric acid ( $\text{H}_2\text{SO}_4$ , 98%) under slowly stirring in ice bath. When the mixed solution turns into atrovirens, 12 g of Potassium Permanganate ( $\text{KMnO}_4$ , 99.9%) will be add into the above solution with continuously stirring for 3h between  $0 \sim 20^\circ\text{C}$ , and later heat up to  $37^\circ\text{C}$  with continuously stirring for 1 h. Next, 160 mL deionized water were added into the mixed solution with continuously stirring for 0.5 h at  $95^\circ\text{C}$ . After the temperature of the solution drops to the ambient

temperature, 400 mL deionized water and 14 mL hydrogen peroxide ( $\text{H}_2\text{O}_2$ , 30%) were added into the above solution. At last, the obtained solution was subjected to centrifugation and freeze-drying.

The reduced graphene oxide (RGO) was obtained by a facile process which the ascorbic acid was used as the reduction of the graphene oxide. At first, the as-synthesized GO sample was dissolved in 50 mL of deionized water (2 mg/mL) under the condition of ultrasound. Then 2.5 mmol of ascorbic acid was added in the above solution in 95 °C water-bath for 2 h. After the reaction was completed, the product was immersed by deionized water repeatedly for a week, followed by freeze-drying.

## 2.2 Fabrication of the $\beta\text{-MnO}_2/\text{RGO}$

The  $\beta\text{-MnO}_2/\text{RGO}$  composite was synthesized by a typical hydrothermal method. First of all, 18 mg of RGO were dissolved in 30 mL deionized water with ultrasound for 30 minutes. Next, 0.316 g (2 mmol) of  $\text{KMnO}_4$  was added into the above solution with continuously stirring for 10 minutes at atmospheric temperature to form a homogeneous solution. After the  $\text{KMnO}_4$  were completely dissolved in the solution, 1.6 mL of HCL (3 M) was added into the above mixture with stirring for 5 minutes. The obtained mixture was then transferred into a 50 mL Teflonlined stainless steel autoclave and heated at 160 °C for 6 h. After the reaction was completed, the autoclave cools to room temperature naturally and the resulting product was washed with distilled water and ethanol several times to get the  $\beta\text{-MnO}_2/\text{RGO}$  composite. The pure  $\beta\text{-MnO}_2$  was synthesized under the same condition except for the addition of RGO, besides the volume of the HCL solution should be changed from 1.6 mL into 3.6 mL, thus we can get the pure  $\beta\text{-MnO}_2$  nanostructure.

## 2.3 Material characterization

The crystal structure analysis of the as-prepared samples was characterized using powder X-ray diffraction (XRD, TD-3500X ) using Cu Ka radiation ( $\lambda=0.154056$  nm).The XRD pattern was recorded in the  $2\theta$  range of 10~80 ° with a scan rate of  $0.07^\circ \text{s}^{-1}$  at an working voltage of 30.0 kV and working current of 200 mA. Raman spectra were recorded using a confocal LabRAM HR800 spectrometer (Horiba Jobin-Yvon, FR.) with an excitation wavelength of 532 nm and frequency swing of 100~4000  $\text{cm}^{-1}$  from an argon ion laser. The chemical compositions of the samples were determined using X-ray photoelectron spectroscopy (XPS) on a Thermo ESCALAB 250XI spectrometer with an Al Ka X-ray source (1486 eV). The morphology and microstructure of the obtained samples were observed on a FEI quanta 250 scanning electron microscopy (SEM) at an operating voltage of 15.0 kV

## 2.4 Electrochemical characterization

CR 2032-type coin cells were used to perform electrochemical measurements, which were assembled in an argon-filled glove box with the concentration of oxygen and water below 0.1 ppm. The working electrodes were prepared by mixing the active material, acetylene black and polyvinylidene fluoride (PVDF) in a weight ratio of 8:1:1 in N-methyl-2-pyrrolidone (NMP) to form

homogeneous slurry. Next, the slurry uniformly coated onto Cu foil and dried at 120 °C for 12 h under vacuum condition. Pure lithium foil was used as the counter electrode and 1 M of LiPF<sub>6</sub> in ethylene carbonate (EC) and dimethyl carbonate (DMC) (1:1 v/v) as the electrolyte.

The galvanostatic charge/discharge tests were carried out on a Neware battery testing system at a scanning rate of 0.2 mV s<sup>-1</sup> in the potential range of 0.01 to 3.0 V at various current densities. Electrochemical impedance spectra (EIS) were collected with a sine-wave amplitude of 5 mV in a frequency range of 0.01 Hz to 100 kHz. The electrochemical performance of the as-synthesized electrodes were measured on a CHI760E electrochemical workstation (shanghai, Chenhua).

### 3. RESULTS AND DISCUSSION

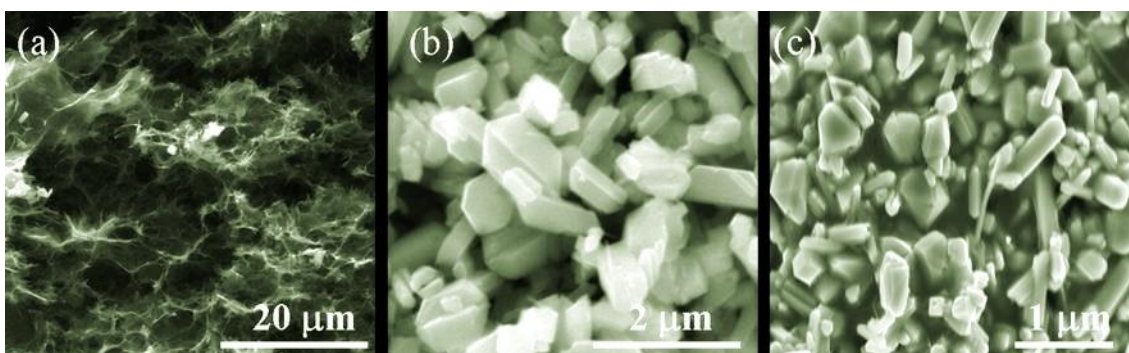


**Figure 1.** SEM Images of (a) RGO, (b) MnO<sub>2</sub> and (c) β-MnO<sub>2</sub>/RGO composite.

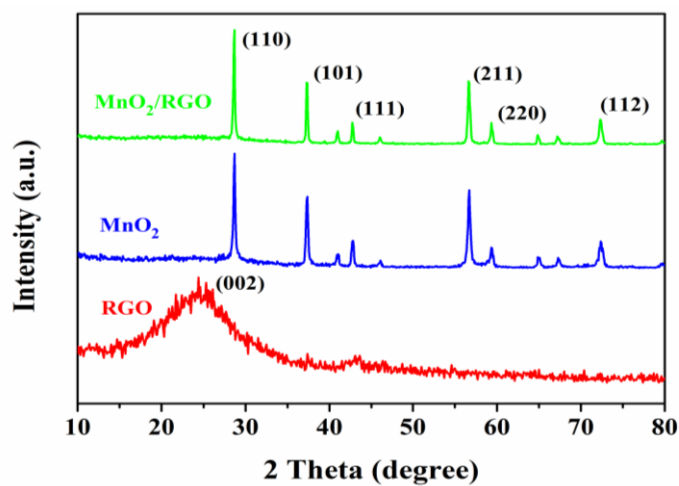


**Figure 2.** Typical XRD patterns of as-prepared RGO, MnO<sub>2</sub> and β-MnO<sub>2</sub>/RGO composite.

The sizes and morphologies of (a) RGO, (b) MnO<sub>2</sub> and (c) β-MnO<sub>2</sub>/RGO nanostructures are characterized by the SEM analysis. As shown in Fig. 1a, the as-synthesized RGO shows a three dimensional net-work structure, which is composed of interconnected graphene nanosheets with porous structure, and the average diameter of the pore structure is estimated to be of submicron to tens

of microns. Fig. 1b shows the anomalous hexagon morphology of the  $\text{MnO}_2$  with a smooth surface, the dispersion of  $\text{MnO}_2$  is well-distributed and there is no obvious phenomenon of agglomeration. According to Fig. 1c, we can very clearly see that on the surface of RGO was tightly covered with  $\text{MnO}_2$ , which will have a positive influence on the lithium storage performance of the composite, due to that the RGO acts as a load material can efficiently buffer the volume expansion of  $\text{MnO}_2$ , shorten the diffusion distance of lithium ion and electron, improve the active site of lithium ion, thus greatly improved the electrochemical performance of the  $\beta\text{-MnO}_2/\text{RGO}$  composite.

The phase purity and crystal structure of the as-prepared samples were examined by XRD. As shown in Fig. 2, the RGO shows a weak and broad diffraction peak (002) of graphite in the range of  $22\text{--}28^\circ$ . This is the same as the previous reports [28,29]. All the peaks of  $\text{MnO}_2$  can be indexed to the planes of the tetragonal structure of  $\beta\text{-MnO}_2$  (JCPDS 24-0735, space group  $P4_2/mnm(136)$ ,  $a=b=4.3999$ ,  $c=2.874$ ). There are no other noticeable impurities, suggesting the sample with a high relatively crystal purity. It also can be observed all the peaks are narrow, which indicates that the as-prepared  $\text{MnO}_2$  has a perfect crystallized structure. The XRD pattern of the as-prepared  $\beta\text{-MnO}_2/\text{RGO}$  composite is the same as the  $\text{MnO}_2$  sample, and no obvious RGO diffraction peaks are found, it attributes to that a large amount of  $\text{MnO}_2$  load on the surface of the RGO and the diffraction peak of RGO is too weak so that it shields the RGO signal.

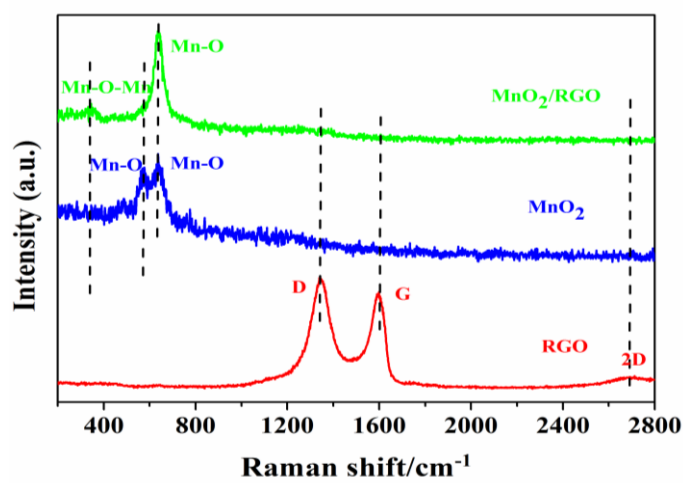


**Figure 3.** Raman spectra of the RGO,  $\text{MnO}_2$  and  $\beta\text{-MnO}_2/\text{RGO}$  composite.

Fig. 3 is the Raman spectra of RGO,  $\text{MnO}_2$  and  $\beta\text{-MnO}_2/\text{RGO}$  composite. As shown in Fig. 3, there are three distinct Raman peaks at  $1342$ ,  $1592$  and  $2711\text{ cm}^{-1}$  for RGO, corresponding to the D peak, G peak and 2D peak, respectively. Among them, the D peak is the defect peak of  $\text{SP}^3$  disordered carbon and RGO surface, the G peak is the basic peak of RGO, and the 2D peak is related to the number of RGO layers [30]. It is found that the intensity ratio of D peak and G peak is 1.17, which is due to the increase of the defect concentration resulting from the reduction of graphene oxide by ascorbic acid. The results further show that the RGO is successfully obtained. In addition, the intensity ratio of G peak and 2D peak is significantly larger than 1, which indicates that the RGO has a multi-layer structure. The  $\text{MnO}_2$  Raman spectrum has two obvious characteristic peaks, which are located in 572

$\text{cm}^{-1}$  and  $630 \text{ cm}^{-1}$ , the peak at  $572 \text{ cm}^{-1}$  roots in the Mn-O stretching vibration of the  $\text{MnO}_6$  planar, and the peak at  $630 \text{ cm}^{-1}$  corresponds to the  $\text{MnO}_6$  based double stranded Mn-O ring stretching vibration[31-33]. No Raman peaks of RGO are found in the Raman spectra of composite materials. At the same time, the Raman peak of  $\beta\text{-MnO}_2/\text{RGO}$  composite is disappeared at  $572 \text{ cm}^{-1}$ , and a new Raman peak appears near  $383 \text{ cm}^{-1}$ , which is caused by the stretching vibration of Mn-O-Mn in  $\text{MnO}_2$ .

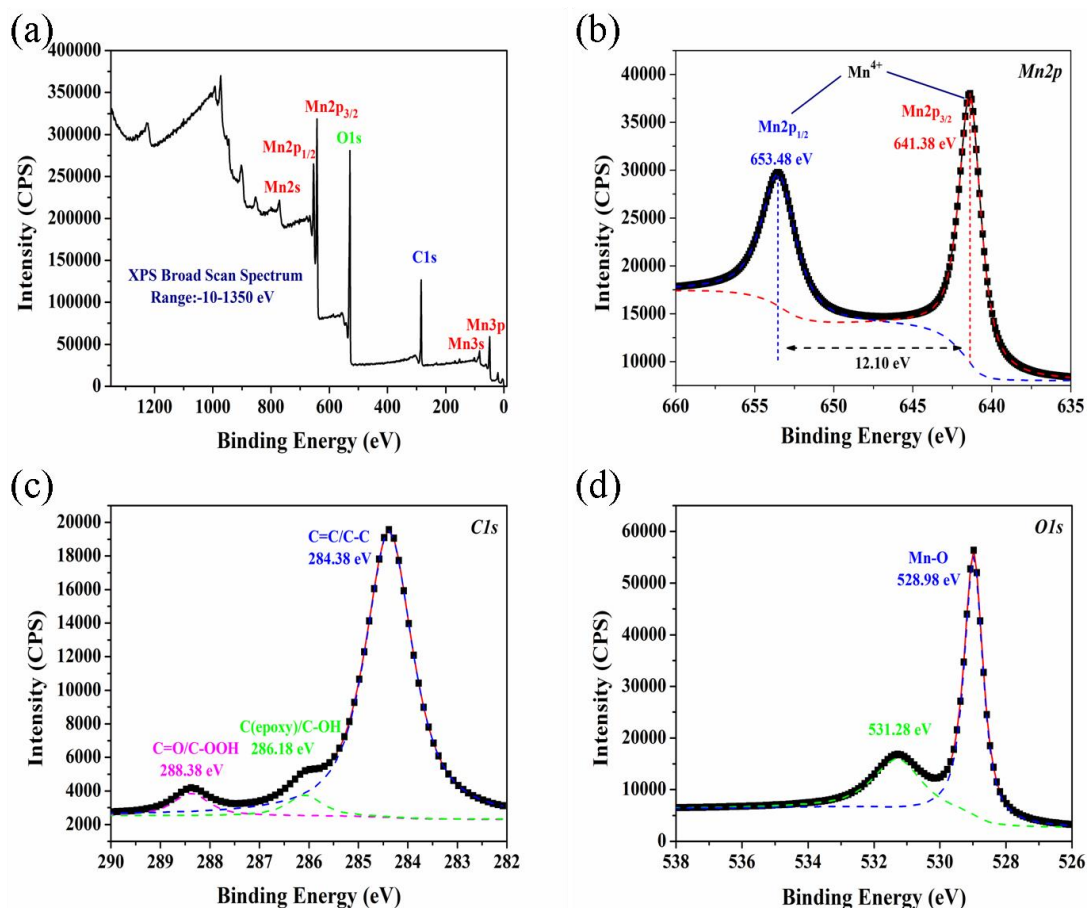


**Figure 4.** XPS survey spectrum (a), the high-resolution Mn2p spectrum(b), the high-resolution C1s spectrum(c) and the high-resolution O1s spectrum(d) of  $\beta\text{-MnO}_2/\text{RGO}$  composite.

XPS analysis was performed to analyze the the element composition of  $\beta\text{-MnO}_2/\text{RGO}$  composite, the surface functional groups types of RGO, and the state of Mn and O in the composite. Fig. 4 is the XPS survey spectrum of  $\beta\text{-MnO}_2/\text{RGO}$ , and the high-resolution spectrum of Mn2p, C1s and O1s, respectively. The XPS survey spectrum of the  $\beta\text{-MnO}_2/\text{RGO}$  composite is shown on Fig. 4a, the characteristic peaks at 104.0 eV, 284.6 eV, 530.3 eV, 711.3 and 852.4 eV corresponding to Mn3p, Mn3s, C1s, O1s, Mn2p<sub>3/2</sub>, Mn2p<sub>1/2</sub> and Mn2s, respectively. It shows that the composite is mainly composed of three elements of Mn, C and O. Fig. 4b is the high-resolution XPS of Mn2p, there are two distinct characteristic peaks in 641.38eV and 653.48eV, which are indexed to Mn2p<sub>3/2</sub> and Mn2p<sub>1/2</sub> of Mn, respectively [34]. And the energy difference between the two characteristic peaks of Mn2p<sub>3/2</sub> and Mn2p<sub>1/2</sub> is 12.1eV, it illustrates that the existence of Mn in the composite material with the form of +4 valence. Fig. 4c is the C1s spectrum of  $\beta\text{-MnO}_2/\text{RGO}$  composite. It can be found

that there are three characteristic peaks in C1s at 284.38, 286.18 and 288.38 eV, respectively, which corresponding to C=C/C-C, epoxy /C-O and C=O/C-OOH functional groups, respectively [35]. The strength of C=C/C-C bond is significantly higher than that of epoxy /C-O and C=O/C-OOH functional groups, which indicates that C in the composite is mainly in the form of C=C/C-C bond. The O1s spectrum of  $\beta$ -MnO<sub>2</sub>/RGO composite is shown in Fig. 4d, the characteristic peaks at 528.98 eV and 531.28 eV correspond to Mn-O bond and Mn-OH, respectively [36]. Based on high resolution XPS spectra of Mn2p and O1s, it can be concluded that the Mn element in the composite is in the form of MnO<sub>2</sub>.

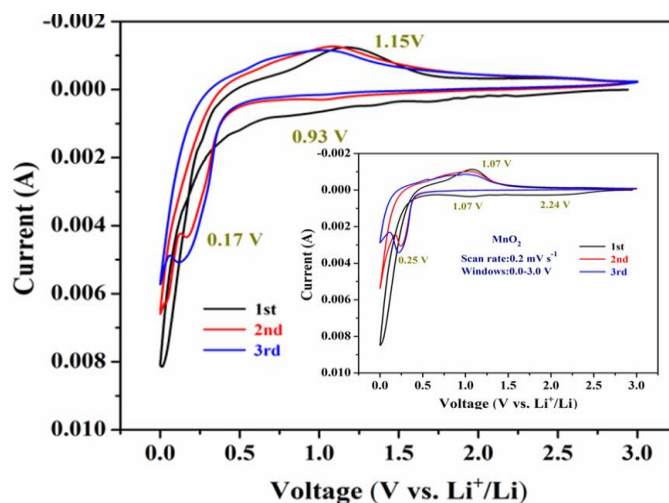


**Figure 5.** Cyclic voltammograms (CV) of  $\beta$ -MnO<sub>2</sub>/RGO composite, inset of CV the bare  $\beta$ -MnO<sub>2</sub>.

Fig. 5 shows the first three CV curves of  $\beta$ -MnO<sub>2</sub>/RGO composite at the scanning rate of 0.2 mV s<sup>-1</sup> in the potential range of 0.01~3.00 V. From the CV curve of  $\beta$ -MnO<sub>2</sub>/RGO composite in Fig. 5, it can be observed that the cyclic voltammetry characteristic curve of the composite is similar to that of MnO<sub>2</sub> (inset of Fig.5), and there is a deviation for the oxidation peaks and reduction peaks of the  $\beta$ -MnO<sub>2</sub>/RGO composite compared to MnO<sub>2</sub>, which can be ascribed to that the lithium ion inserts into the two materials of MnO<sub>2</sub> and graphene at the same time. During the first discharge process, there is a weak reduction peak of  $\beta$ -MnO<sub>2</sub>/RGO composite at around 0.93 V, which corresponds to the formation of solid electrolyte boundary film and the reduction of MnO<sub>2</sub> [14,37]. The peak at around 0.01 V corresponds to the lithium ion inserts into graphene [37]. During the charge process, there is an oxidation peak at 1.15 V, which is caused by the conversion of Mn to MnO<sub>2</sub> [38]. From inset of Fig.5, it can be found that there are two reduction peaks located at 2.24 V and 1.07 V in the first discharge of MnO<sub>2</sub> electrode. The reduction peak at 2.24 V corresponds to the decomposition of the electrolyte on the electrode surface. While the reduction peak located at 1.07 V corresponds to the insertion of lithium ion with the reduction of MnO<sub>2</sub> to elemental Mn and the formation of the solid electrolyte interface film. In the first charging process, there is only one oxidation peak at around 1.07 V, corresponding to the oxidation of elemental Mn to MnO<sub>2</sub> under the action of lithium. During the subsequent cycle process, only a pair of redox peaks at 1.03/0.25 V is found. At the same time, both the oxidation peaks and the reduction peaks move to the left, which is due to the polarization of the

electrode during the charge and discharge process.

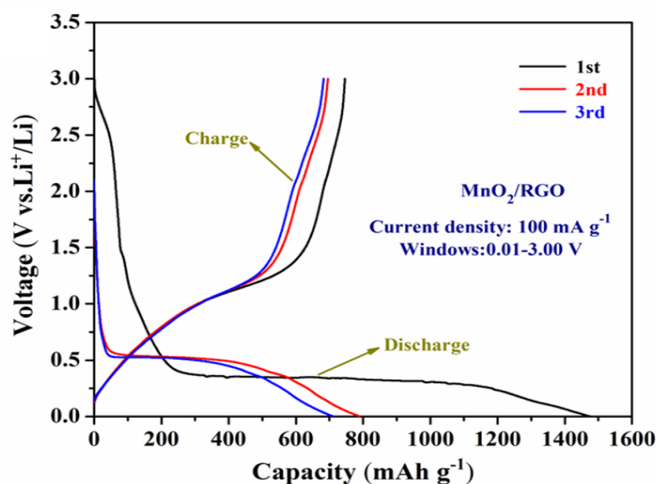


**Figure 6.** galvanostatic charge/discharge profiles of  $\beta$ - $\text{MnO}_2/\text{RGO}$  composite.

The first three galvanostatic charge/discharge profiles of  $\beta$ - $\text{MnO}_2/\text{RGO}$  composite were evaluated at a current density of  $100 \text{ mA g}^{-1}$  in a voltage of  $0.01\sim 3.0 \text{ V}$ . As shown in Fig. 6, In the first cycle,  $\beta$ - $\text{MnO}_2/\text{RGO}$  composite displays a discharge-charge capacity of  $1475/746 \text{ mAh g}^{-1}$ , with coulomb efficiency of  $50.5 \%$ . The initial irreversible capacity loss and the low coulomb efficiency of  $\beta$ - $\text{MnO}_2/\text{RGO}$  composite can be ascribed to the solid electrolyte interface (SEI) layer which is formed on the surface of the electrode material by the decomposition of the electrolyte during the first discharge process [39,40]. In the subsequent two cycles, it can be clearly found that the capacity loss of  $\beta$ - $\text{MnO}_2/\text{RGO}$  composite has a great reduction, which indicates that the cycle stability of the electrode materials is improved.

To further evaluate the cycling performance of RGO,  $\text{MnO}_2$  and  $\beta$ - $\text{MnO}_2/\text{RGO}$  composite electrode materials, charge-discharge testing for 50 cycles at a current density of  $100 \text{ mA g}^{-1}$  in a voltage range of  $0.01\sim 3.0 \text{ V}$  was measured. The relational graph of the discharge capacity and the cycle times are shown in Fig.7, there is a sharp lose of the discharge capacities after the first cycle, and the capacity retention of RGO,  $\text{MnO}_2$  and  $\beta$ - $\text{MnO}_2/\text{RGO}$  is  $49.8\%$ ,  $29.1\%$  and  $53.6\%$ , respectively. The lose rate of the discharge capacities tends to be gentle between 2 to 10 cycles. After the 20th cycle, the capacity retention of RGO,  $\text{MnO}_2$  and  $\beta$ - $\text{MnO}_2/\text{RGO}$  is  $36.3\%$ ,  $9.4\%$  and  $35.4\%$ , respectively. The three electrode materials can still maintain a sustainable reversible capacity of  $337 \text{ mAh g}^{-1}$ ,  $103 \text{ mAh g}^{-1}$  and  $448 \text{ mAh g}^{-1}$  over 50 cycles, and retain a capacity retention of  $34.7\%$ ,  $6.6\%$  and  $34.4\%$ , respectively. Obviously, the discharge capacity and the capacity retention of  $\beta$ - $\text{MnO}_2/\text{RGO}$  composite are much higher than  $262 \text{ mAh g}^{-1}$  of  $\alpha$ - $\text{MnO}_2/\text{RGO}$  composite after 30 cycles for the previous report [41]. The high specific capacity and excellent cycling stability for the  $\beta$ - $\text{MnO}_2/\text{RGO}$  composite can be ascribed to compact ( $1\times 1$ ) tunnel structure of  $\beta$ - $\text{MnO}_2$  and excellent electrical conductivity of RGO. Both the tunnel structure of  $\beta$ - $\text{MnO}_2$  and RGO can effectively accommodate the volume change and improve diffusion paths for both lithium ions and electrons. From the coulomb efficiency curve of the  $\beta$ - $\text{MnO}_2/\text{RGO}$  composite, we can found that it has a low initial coulomb efficiency. Subsequently, the

coulomb efficiency continued to rise and finally up to 99% after 14<sup>th</sup> cycles.

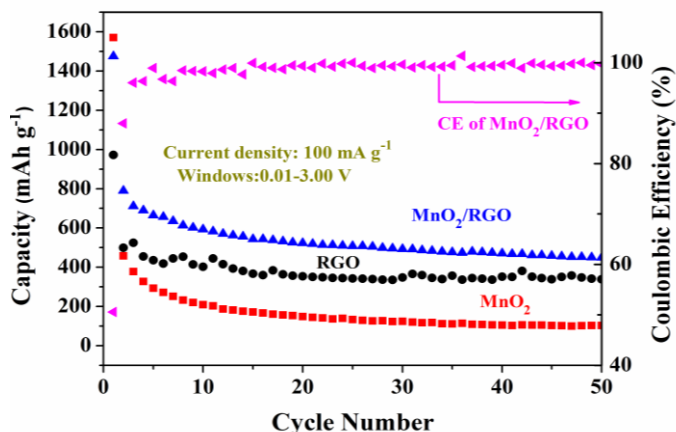


**Figure 7.** Cycling performance of RGO, MnO<sub>2</sub> and β-MnO<sub>2</sub>/RGO composite at a current density of 100 mA g<sup>-1</sup>.

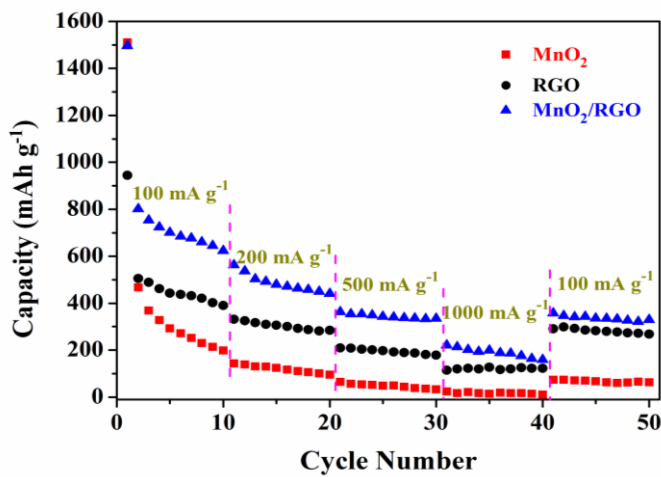


**Figure 8.** Rate performance of RGO, MnO<sub>2</sub> and β-MnO<sub>2</sub>/RGO composite under different current densities.

The discharge capacity curves of RGO, MnO<sub>2</sub> and β-MnO<sub>2</sub>/RGO composite were measured at various rates of 100, 200, and 1000 mA g<sup>-1</sup>. As shown in Fig.8, the rate performance of MnO<sub>2</sub> and β-MnO<sub>2</sub>/MnO<sub>2</sub> composite exist obvious difference, which the composite shows a excellent rate performance and remains a reversible capacity of 159 mAh g<sup>-1</sup> even at the current densities of 1000 mA g<sup>-1</sup> and when the current densities drop to 100 mA g<sup>-1</sup>, it can still retain a reversible capacity of 328 mAh g<sup>-1</sup>, while the pure MnO<sub>2</sub> shows a bad rate performance. The current densities increase from 100 to 1000 mA g<sup>-1</sup>, the reversible capacity of the pure MnO<sub>2</sub> drops from 198 to 9.7 mAh g<sup>-1</sup>, even when the current densities back to 100 mA g<sup>-1</sup>, there is only 63 mAh g<sup>-1</sup> of the reversible capacity left. What makes the differences between the two materials, which can be attributed to that RGO can efficiently

buffer the volume expansion of  $\text{MnO}_2$ , and the porous structure of  $\text{MnO}_2$  is conducive to the transfer of lithium ion and electron, so as to improve the rate performance of the electrodes.

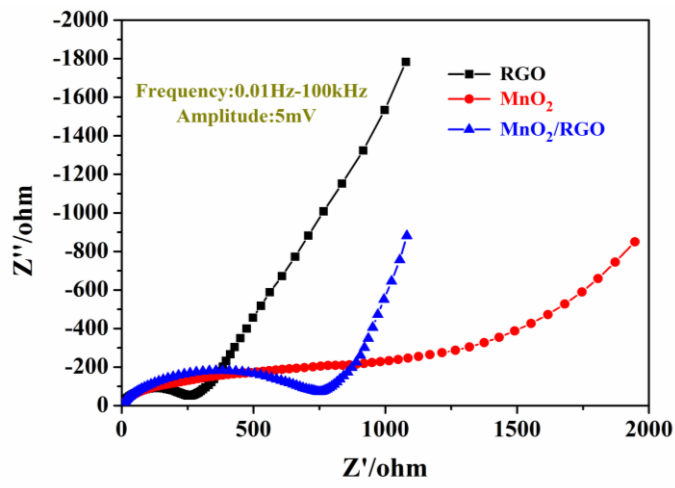


**Figure 9.** Nyquist plots of RGO,  $\text{MnO}_2$  and  $\beta\text{-MnO}_2/\text{RGO}$  composite.

In order to dig out the differences of the conductivity among RGO,  $\text{MnO}_2$  and  $\beta\text{-MnO}_2/\text{RGO}$  composite, we have carried out the electrochemical AC impedance test for the three materials. Fig.9 is the Nyquist plots of RGO,  $\text{MnO}_2$  and  $\beta\text{-MnO}_2/\text{RGO}$  electrodes. The AC impedance spectra of the three different materials is composed of a high-frequency semicircle and low-frequency line, which the semicircle diameter and the electrode contact resistance related to the charge transfer resistance, and the linear slope on behalves of the lithium ion diffusion activity[42]. The smaller semicircle diameter, the better is the electrode conductivity. The larger the slope of the line, the higher is the activity of lithium ion diffusion [29, 42]. It can be seen from Fig.9, the diameter of the semicircle sequence decreases from  $\text{MnO}_2$ ,  $\beta\text{-MnO}_2/\text{RGO}$  to RGO, the slope of the line is increased from  $\text{MnO}_2$ , RGO to  $\beta\text{-MnO}_2/\text{RGO}$  in turn. The results indicate that the  $\beta\text{-MnO}_2/\text{RGO}$  composite has a higher conductivity and lithium ion diffusion activity compared with pure  $\text{MnO}_2$ , thus it has a better electrochemical performance, which dues to the excellent electrical conductivity of RGO.

#### 4. CONCLUSIONS

In summary, we're reporting a facile method to synthesize  $\beta\text{-MnO}_2/\text{RGO}$  composite via hydrothermal. In this composite, RGO not only acts as a reducing agent, but also acts as a load material shows a nearly hexagon morphology. When it was used as anode materials for lithium ion batteries, it exhibits excellent cycling stability and good rate performance dues to the compact ( $1\times 1$ ) tunnel structure of  $\beta\text{-MnO}_2$  and excellent electrical conductivity of RGO. Both the tunnel structure of  $\beta\text{-MnO}_2$  and RGO can efficiently buffer the volume expansion of  $\text{MnO}_2$ , shorten the diffusion distance of lithium ion and electron, thus they greatly improve the active site of lithium ion. The  $\beta\text{-MnO}_2/\text{RGO}$  composite is a good candidate as high-performance anode materials for lithium ion batteries.

## ACKNOWLEDGEMENTS

This work was financially supported by Basic and Frontier Research Program of Chongqing Municipality (cstc2015jcyjA90020) and (cstc2014jcyjA10063) , Scientific and Technological Research Program of Chongqing Municipal Education Commission (KJ1501101), (KJ1500323) and (KJ1501116), China Postdoctoral Science Foundation (2015M582499), Postdoctoral special Foundation of Chongqing (Xm2015064) and Project of Chongqing Normal University (14XYY025), and National Natural Science Foundation of China (51502030).

## References

1. W. Wei, S. Yang, H. Zhou, I. Lieberwirth, X. Feng and K. Muellen, *Adv. Mater.*, 25 (2013) 2909.
2. C. Hsie, . Lin, Y. Chen and J. Lin, *Electrochim. Acta*, 111 (2013) 359.
3. S. Li, Y. Xiao, X. Wang and M. Cao, *Phys. Chem. Chem. Phys.*, 16 (2014) 5846.
4. Z. X. Huang, Y. Wang, Y.G. Zhu, Y. Shi, J.I. Wong and H.Y. Yang, *Nanoscale*, 6 (2014) 9839.
5. Y. Liu , Y. Li, M. Zhong, Y. Hu, P. Hu, M. Zhu, W. Li and Y. Li, *Mater. Lett.*, 171 (2016) 244.
6. D. Zhang, Q. Wang, Q. Wang, J. Sun, L. Xing and X. Xue, *Mater. Lett.*, 128 (2014) 295.
7. H. Wang, G. Wang, S. Yuan, D. Ma, Y. Li and Y. Zhang, *Nano Res.*, 8 (2015) 659.
8. S. Deng, L. Wang, T. Hou and Y. Li, *J. Phys. Chem. C*, 119 (2015) 28783.
9. Y. Zhang, M. Su, L. Ge, S. Ge, J. Yu and X. Song, *Carbon*, 57 (2013) 22.
10. S. Wang, Q.Li, W. Pu, Y. Wu and M. Yang, *J. Alloys Compd.*, 663 (2016) 148.
11. S. Luo, S. Xu, Y. Zhang, J. Liu, S. Wang and P. He, *J. Solid State Electrochem.*, 20 (2016) 2045.
12. Y. Wang, P. Ding and C. Wang, *J. Alloys Compd.*, 654 (2016) 273.
13. M. Hilmy Alfaruqi, J. Gim, S. Kim, J. Song, D. Tung Pham, J. Jo, Z. Xiu, V. Mathew and J.Kim, *Electrochem. Commun.*, 60 (2015) 121.
14. X.Shen, T. Qian, J. Zhou, N. Xu, T. Yang and C. Yan, *ACS Appl. Mater. Interfaces*, 7 (2015) 25298.
15. X. Sun, M. Gan, L. Ma, H. Wang, T. Zhou, S. Wang, W. Dai and H. Wang, *Electrochim. Acta*, 180 (2015) 977.
16. K. Noufel, A. Bouzida, N. Chelalia and L. Zerroual, *Russ. J. Appl. Chem.*, 88 (2015) 1711.
17. Y. Yang and C. Huang, *J. Solid State Electrochem.*, 14 (2010) 1293.
18. X. Guo, L. Cong, Q. Zhao, L. Tai, X. Wu, J. Zhang, R. Wang, H. Xie and L. Sun, *J. Alloys Compd.*, 651 (2015) 12.
19. C. Wei, H. Pang, B. Zhang, Q. Lu, S. Liang and F. Gao, *Sci. Rep.*, 3 (2013) 1.
20. M. Wang, Q. Yang, T. Zhang, B. Zhu and G. Li, *Rsc Adv.*, 6 (2016) 19952.
21. W. Mao, G. Ai, Y. Dai, Y. Fu, Y. Ma, S. Shi, R. Soe, X. Zhang, D. Qu, Z. Tang and V. Battaglia, *J. Power Sources*, 310 (2016) 54.
22. Y. Zhang, Q. Xiao, G. Lei and Z.i Li, *Phys. Chem. Chem. Phys.*, 17 ( 2015) 18699.
23. T. Gu and B. Wei, *Nanoscale*, 7 (2015) 11626.
24. J. Zhang, J. Feng, T., Z.Liu, Q. Li, S. Chen and C. Xu, *Electrochim. Acta*, 196 (2016) 661.
25. D. Sun, J. Chen, J. Yang and X. Yan, *Crystengcomm*, 16 (2014) 10476.
26. K. Wen, G. Chen, F. Jiang, X. Zhou and J. Yang, *Int. J. Electrochem. Sci.*, 10 (2015) 3859.
27. B. Zhao, Y. Xu, S. Huang, K.Zhang, M. M.F. Yuen, J. Xu X. Fu, R. Sun and C. Wong, *Electrochim. Acta*, 202 (2016) 186.
28. S.K. Park, H.J. Lee, M.H. Lee and H.S. Park, *Chem. Eng. J.*, 281 (2015) 724.
29. H. Tao, L. Fan, Y. Mei and X. Qu, *Electrochem. Commun.*, 13 (2011) 1332.
30. J. Ding, B. Li, Y. Liu, X. Yan, S. Zeng, X. Zhang, L. Hou, Q. Cai and J. Zhang, *J. Mater. Chem. A*, 3 (2015) 832.
31. G.G. Kumar, Z. Awan, K.S. Nahm and J.S. Xavier, *Biosens. Bioelectron.*, 53 (2014) 528.
32. H. Zhao, F. Liu, G. Han, Z. Liu, B. Liu, D. Fu, Y. Li and M. Li, *J. Solid State Electrochem.*, 18 (2014) 553.

33. M. Hu, K.S. Hui and K.N. Hui, *Chem. Eng. J.*, 254 (2014) 237.
34. L. Li, A.-R.O. Raji and J.M. Tour, *Adv. Mater.*, 25 (2013) 6298.
35. X. Li, X. Huang, D. Liu, X. Wang, S. Song, L. Zhou and H. Zhang, *J. Phys. Chem. C*, 115 (2011) 21567.
36. K. Dai, L. Lu, C. Liang, J. Dai, Q. Liu, Y. Zhang, G. Zhu and Z. Liu, *Electrochim. Acta*, 116 (2014) 111.
37. Y.C. Dong, R.G. Ma, M.J. Hu, H. Cheng, C. K. Tsang, Q.D. Yang, Y.Y. Li and J.A. Zapien, *J. Solid State Electrochem.*, 201 (2013) 330.
38. L. Xing, C. Cui, C. Ma and X. Xue, *Mater. Lett.*, 65 (2011) 2104.
39. Z. Yan, L. Liu, H. Guo, J. Tan, H. Shu, X. Yang, H. Hu, Q. Zhou, Z. Huang and X. Wang, *Electrochim. Acta*, 123 (2014) 551.
40. X. Wang, Y. Wang, L. Yang, K. Wang, X. Lou and B. Cai, *J. Power Sources*, 262 (2014) 72.
41. Y.H. Zhao, G. Chen, D. Wang, C.L. Song, L.P. Xie, L. Chang, R. Wang and N.L. Zhong, *Int. J. Electrochem. Sci.*, 11 (2016) 2525.
42. H. Liu, J. Huang, X. Li, J. Liu and Y. Zhang, *Ceram. Int.*, 38 (2012) 5145.

© 2016 The Authors. Published by ESG ([www.electrochemsci.org](http://www.electrochemsci.org)). This article is an open access article distributed under the terms and conditions of the Creative Commons Attribution license (<http://creativecommons.org/licenses/by/4.0/>).